Citation: G. López-Nicolás, J. J. Guerrero, and C. Sagüés. Visual control of vehicles using two-view geometry. Mechatronics, vol. 20, no. 2, pp. 315-325, 2010

Visual Control of Vehicles Using Two-View Geometry

G. López-Nicolás, J.J. Guerrero and C. Sagüés

Dept. Informática e Ingeniería de Sistemas - Instituto de Investigación en Ingeniería de Aragón, Universidad de Zaragoza, Spain
{gonlopez, jguerrer, csagues}@unizar.es

Abstract

This paper addresses the problem of visual control for mobile robots with nonholonomic motion constraints. The vision system consists of a fixed camera mounted on the robot and no odometry or additional sensors are used. We consider the usual framework in which the target is defined by an image taken previously at the desired position. Then, the control law drives the robot from the initial position to the desired one by processing image information extracted from the current and target images. We present a new approach consisting in a switching control law based on the two-view geometry without scene constraints. Our main contribution is that two controllers are defined and combined in the switching control law. One is based on the epipolar geometry and the other on the homography model. Both models have well known degenerate cases or particular situations in which the corresponding control fails when used alone. Nevertheless, the designed approach takes advantage of both models avoiding the drawbacks of each one and allowing a smooth motion of the robot. Experimental evaluation is presented to show the performance of the approach.

1 Introduction

In the last decades, much work has already been accomplished in the area of vision for mobile robot navigation [1] [2]. In general, integrating information from different sensors increases the versatility of the system, but also the cost and the complexity. Vision is one of the most studied sensory modalities for navigation purposes standing out because it provides rich information of the environment. The framework of the approach presented in this paper is a

[1] This work was supported by projects DPI2009-08126 and DPI2009-14664-C02-01.

vision system consisting of a fixed camera mounted on a mobile robot. The visual control task uses the classical idea of homing, also known as teach-by-showing. In this approach, an image is taken previously at the desired position, and then, the control compares the current image with the target one, and an error control vector is extracted from the two views. The robot is led to the target by the controller while the error is reduced to zero implying that the robot has reached the desired position. Visual control methods can be classified depending on how the visual information is used to perform the task. Image data can be used directly (image-based methods [3–10]); it can be used to compute estimates of pose parameters (position-based methods [11–13]); or various combinations of these approaches can be used (hybrid or partitioned methods [14–16]). A traditional approach is to perform the navigation by computing the epipolar geometry between the current image and the target one [11, 17–19]. Nevertheless, the estimation of the epipolar geometry degenerates with short baseline and becomes ill-conditioned for planar scenes. A natural way to overcome this problem is by using the homography model [13, 20, 21]. Nevertheless, if no plane is detected in the scene, the homography-based control fails. This problem can be solved through virtual planes [22], but estimations based on virtual planes with wide baseline are not robust to mismatches, noise or occlusions.

Here, we propose a new approach consisting in a switching control based on the epipolar geometry and the homography. Both individual controllers are obtained through an exact input-output linearization of the correspondent geometric model, transforming the nonlinear control problem into a tracking problem. The resultant robot motion depends on the definition of the desired trajectories of the model parameters. In one case the control inputs are the epipoles and in the other case the homography elements. The work presented in [19, 24] is the basis of the epipolar-based control presented here. In those works, the motion is performed in three sequential steps. However, the motion performed in the second step drives the robot from and not to the target before turning back to it in the final step, which is not the intuitive behaviour we might expect. This behaviour is improved in [18, 23] resulting in a direct, although non-smooth, motion towards the target. The control scheme presented here is intended for producing a smooth motion. On the other hand, the homography-based control presented extends the previous work [25] by designing a new set of trajectories of the homography elements using sinusoids. The approach presented takes advantage of both the epipolar and homography-based methods in a new switching model-based control scheme. This switching control overcomes the particular drawbacks of the epipolar and the homography-based controllers resulting in a more robust and general control scheme.

The remainder of this paper is structured as follows. Section 2 gives the robot motion and camera models. The epipolar-based control and the homography-

based control are presented in Sections 3 and 4, respectively. The combination of these controllers gives the switching control law presented in Section 5. Stability analysis and experimental evaluation are given in Sections 6 and 7, respectively.

2 Robot Motion and Camera Models

The system to be controlled is a nonholonomic robot (Fig. 1(a)) whose dynamics together with a camera model is expressed in a general way as

$$\begin{cases} \dot{\mathbf{x}} = \mathbf{f}(\mathbf{x}, \mathbf{u}) \\ \mathbf{y} = \mathbf{h}(\mathbf{x}) \end{cases} \tag{1}$$

where $\mathbf{x}$ denotes the state vector, $\mathbf{u}$ the system input vector consisting of the robot velocities, and $\mathbf{y}$ the output vector. The general nonholonomic kinematics of a unicycle-like robot expressed in state space is defined as

$$\begin{pmatrix} \dot{x} \\ \dot{z} \\ \dot{\phi} \end{pmatrix} = \begin{pmatrix} -\sin\phi \\ \cos\phi \\ 0 \end{pmatrix} v + \begin{pmatrix} 0 \\ 0 \\ 1 \end{pmatrix} \omega \tag{2}$$

being (x, z, ϕ) the position and orientation of the robot in the global reference (Fig. 1(b)). Thus, the state vector of the robot is $\mathbf{x} = (x, z, \phi)^T$, and the system input vector is defined by the translational (v) and rotational (ω) velocities.

Consider the geometry of the camera to be modelled by perspective projection. And let us suppose the two images (the current and target) are obtained with the same camera, being $\mathbf{R}$ the rotation and $\mathbf{c}$ the translation between the current and target positions. The internal camera calibration matrix $\mathbf{K}$ is defined by the focal length of the camera α_x and α_y in terms of pixel dimensions in the x and y direction respectively [26]. In practice, we assume that the principal point is in the center of the image ($x_0 = 0$, $y_0 = 0$) and that there is no skew.

3 Epipolar-Based Control

In this Section we describe the epipolar-based control law. First, the epipolar geometry model is presented and next, the control law is obtained by the exact

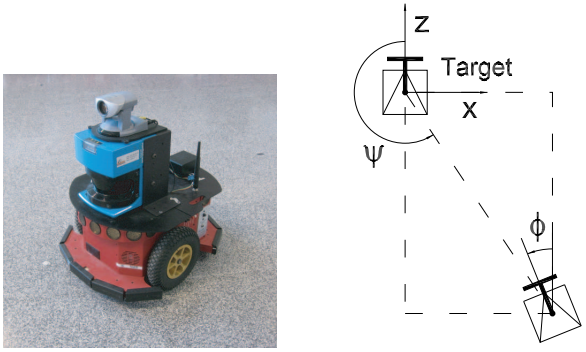

(a) (b)

Fig. 1. (a) The experimental platform. (b) Coordinate system. The robot position is determined by (x, z, ϕ), with ϕ the orientation of the robot, expressed as the angle between the robot body z-axis and the world z-axis. We also define $\psi = -\arctan(x/z)$.

input-output linearization of the system. Finally, the desired trajectories of the epipoles used as control inputs are defined by means of sinusoidal functions.

3.1 The Epipolar Geometry Model

The epipolar geometry represents the intrinsic geometry between two views. It is independent of the scene structure and only depends on the relative localization between the cameras ($\mathbf{R}$, $\mathbf{c}$) and the internal camera parameters ($\mathbf{K}$). The fundamental matrix $\mathbf{F} \in \mathbb{R}^{3\times3}$ is the algebraic representation of this intrinsic geometry. The fundamental matrix satisfies the *epipolar constraint* $\mathbf{p}_2^T\mathbf{F}\mathbf{p}_1 = 0$, where $\mathbf{p}_1$ and $\mathbf{p}_2$ is a pair of corresponding points (Fig. 2(a)), and it can be computed from matched points solving a linear system of equations [26]. The epipoles are the intersections of the baseline, the line joining the optical centers of the cameras $\mathbf{C}_1$ and $\mathbf{C}_2$, with the image planes. They can be computed with $\mathbf{F}\mathbf{e}_1 = \mathbf{0}$ or $\mathbf{F}^T\mathbf{e}_2 = \mathbf{0}$.

In our framework the robot moves with planar motion and only the x-coordinates of the epipoles need to be considered for the control design. From the perspective projection (Fig. 2(b)), the x-coordinate of the epipoles in the current image (e_{cx}) and in the target image (e_{tx}) can be expressed as a function of the state of the robot

$$\begin{cases} e_{cx} = \alpha_x \tan(\phi - \psi) \\ e_{tx} = -\alpha_x \tan(\psi) \end{cases} \tag{3}$$

Then, the output vector of the system (1) is defined with the current and

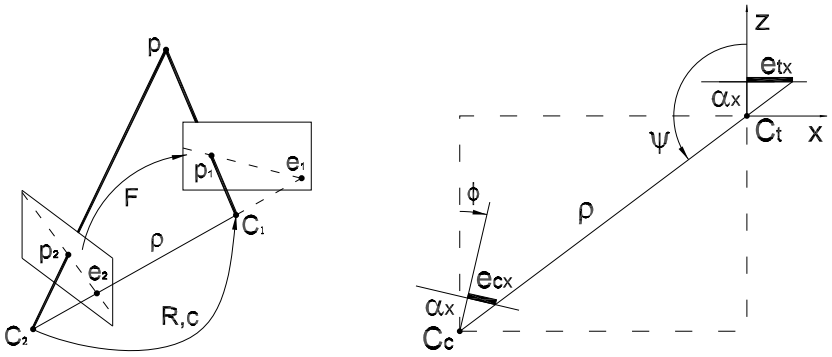

(a) (b)

Fig. 2. (a) The epipolar geometry between two views. (b) Geometric relations of the epipoles in the current image (e_{cx}) and target image (e_{tx}), the epipoles are highlighted in bold line. $\mathbf{C}_c$ and $\mathbf{C}_t$ are the current and target camera positions respectively. (x, z, ϕ) is the robot position in Cartesian coordinates and (ρ, ψ, ϕ) in polar coordinates, where $x = -\rho \sin\psi$ and $z = \rho \cos\psi$.

target epipoles as $\mathbf{y} = (e_{cx}, e_{tx})^T$.

3.2 Input-Output Linearization through the Epipoles

A common way to face the problem of nonlinear control is through linearization [27, 28]. The objective is to perform the navigation by using a feedback control law where the control input is based on the coordinates of the epipoles. Then, the visual servoing problem is transformed into a tracking problem in a nonlinear system where the reference trajectories of the epipoles are defined. The input-output linearization of this work is carried out as originally presented in [24] by differentiating the system outputs until the inputs appear explicitly, and then solving for the control inputs. In that work, the control presented drives a differential drive robot away the target while the lateral error is corrected. After that, the robot moves backwards in a straight line towards the target. In [18] we defined a new control input in such a way that the robot follows a straight line path directly towards the target. The control proposed now is intended for performing a smooth motion towards the target.

The derivatives of the epipoles, in the current and target images (3), are obtained and we have in Table 1 $\dot{e}_{cx}$ and $\dot{e}_{tx}$. With these expressions we have a linear relation between the velocities and the differentiated system output. We solve for the robot velocities v_F and ω_F (Table 1) where subindex F denotes that they have been computed using the epipolar-based control. The control matrix is given by $\mathbf{L_F}^{-1}$ (Table 1).

Now, the new control input $\boldsymbol{\nu}_F$ is defined as a function of the tracking error $\mathbf{e}_F$ of the current and target epipoles. Assuming the control objective to be

Table 1
Equations of the control design developed in the input-output linearization for the epipolar-based control (Section 3.2) and homography-based control (Section 4.2). Refer to the text for explanation about the expressions.

Epipolar-based control	Homography-based control
$\dot{e}_{cx} = -\frac{\alpha_x \sin(\phi-\psi)}{\rho \cos^2(\phi-\psi)}\ v + \frac{\alpha_x}{\cos^2(\phi-\psi)}\ \omega$ $\dot{e}_{tx} = -\frac{\alpha_x \sin(\phi-\psi)}{\rho \cos^2 \psi}\ v$	$\dot{h}_{13} = \alpha_x\ h_{33}\ \omega$ $\dot{h}_{33} = \frac{n_z}{d_\pi}\ v - \frac{h_{13}}{\alpha_x}\ \omega$
$(v_F\,,\ \omega_F)^T = \mathbf{L_F}^{-1} \boldsymbol{\nu}_F$	$(v_H\,,\ \omega_H)^T = \mathbf{L_H}^{-1} \boldsymbol{\nu}_H$
$\mathbf{L_F}^{-1} = \frac{1}{\alpha_x} \begin{bmatrix} 0 & -\frac{\rho \cos^2(\psi)}{\sin(\phi-\psi)} \\ \cos^2(\phi-\psi) & -\cos^2(\psi) \end{bmatrix}$	$\mathbf{L_H}^{-1} = \begin{bmatrix} \frac{h_{13}}{\alpha_x^2 h_{33}} \frac{d_\pi}{n_z} & \frac{d_\pi}{n_z} \\ \frac{1}{\alpha_x h_{33}} & 0 \end{bmatrix}$
$\boldsymbol{\nu}_F = (\nu_c\,,\ \nu_t)^T = \dot{\mathbf{D}}_F - \mathbf{k}_F \mathbf{e}_F$	$\boldsymbol{\nu}_H = (\nu_{13}\,,\ \nu_{33})^T = \dot{\mathbf{D}}_H - \mathbf{k}_H \mathbf{e}_H$
$\mathbf{D}_F = (e^d_{cx}\,,\ e^d_{tx})^T$	$\mathbf{D}_H = (h^d_{13}\,,\ h^d_{33})^T$
$\mathbf{e}_F = (e_{cx} - e^d_{cx}\,,\ e_{tx} - e^d_{tx})^T$	$\mathbf{e}_H = (h_{13} - h^d_{13}\,,\ h_{33} - h^d_{33})^T$
$\mathbf{k}_F = diag(k_c\,,\ k_t)$	$\mathbf{k}_H = diag(k_{13}\,,\ k_{33})$

the tracking of the desired trajectories $\mathbf{D}_F$ of the epipoles, we can compute $\boldsymbol{\nu}_F$ (Table 1), where $k_c > 0$ and $k_t > 0$ are the control gains. The desired functions to be tracked are bounded by definition (section 3.3), and the control inputs designed for the tracking controller are known to represent an exponentially stable error dynamics [28], so the tracking error converges to zero exponentially. This control law needs the matrix $\mathbf{L_F}$ to be invertible. From $det(\mathbf{L_F}) = 0$ we have that the matrix $\mathbf{L_F}$ is singular if $(\phi - \psi) = n\,\pi$ with $n \in \mathbb{Z}$, which is equivalent to $e_{cx} = 0$. This situation can be easily detected and avoided by switching to the other model control law.

3.3 Desired Trajectories of the Epipoles

The desired trajectories of the control input to be tracked determine the path followed by the robot. In [18] the desired trajectories of the epipoles drive a robot with differential motion constraints to follow a straight line path. Here we define a new set of desired trajectories using sinusoidal functions resulting in a smooth motion of the robot. Sinusoidal functions have been already used in motion planning [29] and they gather all the good qualities required by the robot system control. For that purpose, the desired trajectories to regulate the epipoles to zero are defined as

$$\begin{cases} e^d_{cx}(T_1 < t \leq T_2) = \frac{e_{cx}(T_1)}{2} \left(1 + \cos \frac{\pi(t-T_1)}{T_2-T_1}\right) \\ e^d_{cx}(T_2 < t < \infty) = 0 \end{cases} \tag{4}$$

$$\begin{cases} e^d_{tx}(T_1 < t \leq T_2) = \frac{e_{tx}(T_1)}{2}\left(1 + \cos\frac{\pi(t-T_1)}{T_2-T_1}\right) \\ e^d_{tx}(T_2 < t < \infty) = 0 \end{cases} \tag{5}$$

The starting time is $T_1 = 0$ and the desired values of the epipoles are reached in T_2. However, we could find particular situations where the previous motion cannot be performed directly. For example, if the initial robot orientation is the same as the target orientation with $x \neq 0$, the lateral distance would not be corrected by the control. In these cases, a previous phase is performed and the robot is driven with some sinusoids ($0 \leq t \leq T_1$) to an orientation where the previous strategy works properly:

$$\begin{cases} e^d_{cx}(0 \leq t \leq T_1) = e_{cx}(0) + \left(e^d_{cx}(T_1) - e_{cx}(0)\right)\sin\left(\frac{\pi t}{2T_1}\right) \\ e^d_{tx}(0 \leq t \leq T_1) = \frac{e_{tx}(0)+e^d_{tx}(T_1/2)}{2} + \frac{e_{tx}(0)-e^d_{tx}(T_1/2)}{2}\cos\left(\frac{2\pi t}{T_1}\right) \end{cases} \tag{6}$$

In $0 \leq t \leq T_1$ the main parameter to be regulated is the current epipole, related with the robot orientation, while the target epipole value is indifferent. Thus, a rotation is carried out by defining the desired current epipole proportionally to the initial target epipole, $e^d_{cx}(T_1) = -e_{tx}(0)/2$. If we considered differential motion constraints, the desired target epipole trajectory could be defined as $e^d_{tx}(T_1) = e_{tx}(0)$ and then the robot will rotate over its vertical axis during $0 \leq t \leq T_1$. This pure rotation can be avoided with a forward motion by increasing the value of the target epipole. Thus, we define $e^d_{tx}(T_1/2)$ with an increment over the initial epipole $e_{tx}(0)$. In practice we increment it in a 10%, which is related with the bounded curvature constraint. A lower curvature constraint of the vehicle allows a lower increment of $e^d_{tx}(T_1/2)$ and a higher value of $e^d_{tx}(T_1/2)$ requires higher curvature capability, saturating the rotation angle otherwise. We can check if this previous phase (6) is needed and skip it otherwise with the condition: $(e_{cx}(0) \cdot e_{tx}(0)) \leq 0 \Rightarrow T_1 = 0$. It uses the signs of the initial epipoles to check qualitatively the relative orientation of the robot at the beginning of the motion.

Three simulations of this control law are superposed in Fig. 3. The desired trajectories of the current and target epipoles are shown with the resultant paths. This control law presents some drawbacks. The method corrects the lateral error and the orientation of the robot but only reduces depth error (See final $z \neq 0$ in Fig. 3(c)). At the end of the motion the epipoles become undefined because short baseline and the control matrix becomes singular. Besides, the fundamental matrix is ill-conditioned with planar scenes, which are very common in human environments. Therefore, we propose an additional procedure to switch with, which complements this control and avoids these drawbacks.

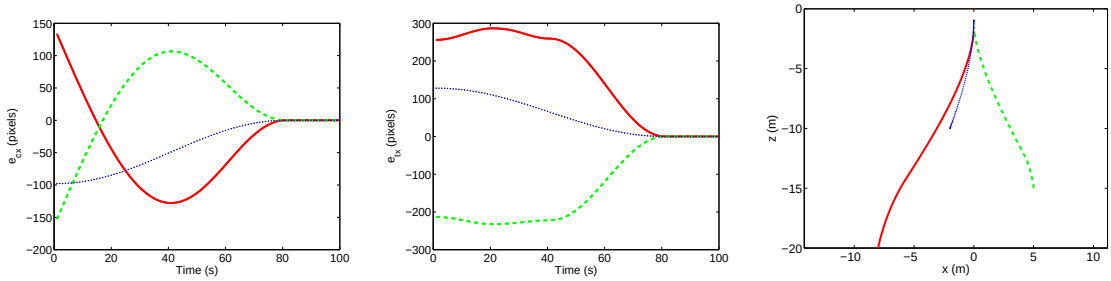

(a) Current epipole (b) Target epipole (c) Paths

Fig. 3. Evolution of the epipoles for three different initial positions and the resultant paths using the epipolar-based control law. The initial positions are $(-8, -20, -10°)$, $(5, -15, 5°)$ and $(-2, -10, -20°)$ and the target is $(0, 0, 0°)$. Each of the simulations is drawn with a different line style. In these simulations $T_1 = 40s$ and $T_2 = 80s$.

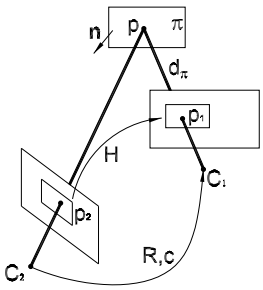

Fig. 4. Homography from a plane between two views.

4 Homography-Based Control

In this Section the homography-based control is presented. First, the homography model for planar motion is described and next, the exact input-output linearization of the system is detailed. The idea is to design the control using directly the homography matrix elements as output of the system [25], avoiding the need of depth estimation or homography decomposition. Finally the desired trajectories of the homography elements used in the control are defined.

4.1 The Homography Model

Two perspective images can be geometrically linked through a plane π of the scene by a homography $\mathbf{H} \in \mathbb{R}^{3\times3}$. This projective transformation $\mathbf{H}$ relates up to scale corresponding points of the plane projected in two images by $\mathbf{p}_2 = \mathbf{H}\,\mathbf{p}_1$ (Fig. 4). The homography across two views can be computed by solving a linear system from a set of point matches [26]. The homography $\mathbf{H}$

can be related to camera motion and plane location as follows

$$\mathbf{H} = \mathbf{K}\mathbf{R}\,(\mathbf{I} + \mathbf{c}\,\frac{\mathbf{n}^T}{d_\pi})\,\mathbf{K}^{-1}\,, \tag{7}$$

where $\mathbf{n} = (n_x,\, n_y,\, n_z)^T$ is the normal to the plane π and d_π is the distance from the origin to the plane. We consider a mobile robot moving in a planar ground (Fig. 1), and the planar motion constraint yields:

$$\mathbf{H} = \begin{bmatrix} h_{11} & h_{12} & h_{13} \\ 0 & 1 & 0 \\ h_{31} & h_{32} & h_{33} \end{bmatrix},\ \text{with}\ \mathbf{R} = \begin{bmatrix} \cos\phi & 0 & \sin\phi \\ 0 & 1 & 0 \\ -\sin\phi & 0 & \cos\phi \end{bmatrix} \text{and}\ \mathbf{c} = \begin{pmatrix} x \\ 0 \\ z \end{pmatrix}. \tag{8}$$

It can be seen that h_{21}, h_{22} and h_{23} do not give information because of the planar motion constraint. Given that h_{22} is never zero we can always normalize the homography to $h_{22} = 1$. Developing expression (7) we obtain the homography elements as a function of the system parameters:

$$\begin{cases} h_{11} = \cos\phi + (x\cos\phi + z\sin\phi)\frac{n_x}{d_\pi} \\ h_{12} = \frac{\alpha_x}{\alpha_y}(x\cos\phi + z\sin\phi)\frac{n_y}{d_\pi} \\ h_{13} = \alpha_x\left(\sin\phi + (x\cos\phi + z\sin\phi)\frac{n_z}{d_\pi}\right) \\ h_{31} = \frac{1}{\alpha_x}\left(-\sin\phi + (-x\sin\phi + z\cos\phi)\frac{n_x}{d_\pi}\right) \\ h_{32} = \frac{1}{\alpha_y}(-x\sin\phi + z\cos\phi)\frac{n_y}{d_\pi} \\ h_{33} = \cos\phi + (-x\sin\phi + z\cos\phi)\frac{n_z}{d_\pi} \end{cases} \tag{9}$$

The analysis of these elements of the homography lead to the design of the control law. Two elements of the homography are enough to control the two degrees of freedom of the system. Elements h_{31} and h_{32} are discarded because they are small compared with the rest of the elements, this is because of the factors α_x and α_y. Then, their ranges are lower than the other elements and they are more affected by noise. This analysis is supported by experimental observations [30]. In our monocular system, planes in front of the robot with dominant n_z will be detected more easily. Thus, from the elements left, we have selected those depending on n_z (i.e. h_{13} and h_{33}). So, the output vector of the system (1) has been defined and it turns out: $\mathbf{y} = (h_{13}, h_{33})^T$.

4.2 Input-Output Linearization through the Homography

We have a nonlinear geometric model relating inputs and outputs. A linearization is developed by differentiating the homography elements until we can solve for the control outputs. Note that the normal vector of the plane ($\mathbf{n}$) and the distance between the plane and the origin (d_π) are referred to the global reference attached at the target position. Given that the target is fixed, these parameters ($\mathbf{n}, d_\pi$) are constant, and their derivatives are zero. The derivatives of h_{13} and h_{33} with respect to time give $\dot{h}_{13}$ and $\dot{h}_{33}$ (Table 1). With these expressions we have a linear relation between the velocities and the differentiated elements of the homography. We solve for the robot velocities v_H and ω_H (Table 1) where subindex H denotes that they have been computed using the homography-based control. The control matrix is given by $\mathbf{L_H}^{-1}$.

The new input of the control $\boldsymbol{\nu}_H$ is given as a function of the tracking error $\mathbf{e}_H$, i.e. the current values of the homography elements $(h_{13}, h_{33})^T$ and their desired values $\mathbf{D}_H$ which are the trajectories to be followed. Then, we define $\boldsymbol{\nu}_H$ (Table 1), where $k_{13} > 0$ and $k_{33} > 0$ are the control gains. The tracking error from the new control input results in an exponentially stable error dynamics [28]. The computation of the control matrix needs $\mathbf{L_H}$ to be invertible.

Proposition 4.1 *In the system state-space, it holds that* $det(\mathbf{L_H}) \neq 0$. *Consequently, the decoupling matrix of the homography-based control is not singular.*

Proof The condition $det(\mathbf{L_H}) \neq 0$ holds if $n_z \neq 0$ and $h_{33} \neq 0$. Without loss of generality we can consider that the plane that generates the homography is at a finite distance to the target and therefore $d_\pi \neq \infty$. We have $n_z \neq 0$ because the plane that generates the homography has to be seen by the camera. When the robot reaches the target position ($\mathbf{x}$=$\mathbf{0}$), we have $h_{33} = 1$. Next, we show that h_{33} is never zero. From (9) we have defined the continuous function

$$h_{33} = \cos\phi - x\frac{n_z}{d_\pi}\sin\phi + z\frac{n_z}{d_\pi}\cos\phi \; .$$

The target is in front of the robot and therefore $z < 0$. The camera field of view is constrained and we can assume $|\phi| < \pi/2$. In our reference system we have that $\cos\phi > 0$ and, given that $n_z < 0$, $z\frac{n_z}{d_\pi}\cos\phi > 0$. Then, it follows that $h_{33} > 0$ if $|\cos\phi + z\frac{n_z}{d_\pi}\cos\phi| > |-x\frac{n_z}{d_\pi}\sin\phi|$. This previous inequality always holds as we consider depth error higher than lateral error ($|z\cos\phi| > |x\sin\phi|$). If this did not hold the robot should carry out a previous manoeuvre due its motion and visibility constraints. Given these results we have that $det(\mathbf{L_H}) \neq 0$ and therefore the control matrix $\mathbf{L_H}$ of the homography-based control is not singular. □

When the target position is reached, the homography is the identity matrix and the desired final values of the homography elements used in the control are $h_{13} = 0$ and $h_{33} = 1$. Now we propose the desired trajectories (h_{13}^d, h_{33}^d) to be tracked determining the path followed by the robot. Basically, although they are not decoupled, we can relate h_{33} with the motion along z-axis and h_{13} with the robot orientation. The selected trajectory for h_{33} is a sinusoid that converges to 1 guaranteeing that the depth distance is corrected. The desired trajectory of h_{13} is defined in order to ensure that it evolves in such a way that lateral and orientation error are corrected simultaneously. Thus, the functions proposed to be tracked are defined as follows

$$\begin{cases} h_{13}^d(T_1 < t \leq T_2) = h_{13}(T_1)\frac{\psi(t)}{\psi(T_1)} \\ h_{13}^d(T_2 < t < \infty) = 0 \end{cases} \tag{10}$$

$$\begin{cases} h_{33}^d(0 \leq t \leq T_2) = \frac{h_{33}(0)+1}{2} + \frac{h_{33}(0)-1}{2}\cos\left(\frac{\pi t}{T_2}\right) \\ h_{33}^d(T_2 < t < \infty) = 1 \end{cases} \tag{11}$$

The starting time is $T_1 = 0$ and the desired homography values are reached in T_2. There are particular initial positions in which the robot needs to be driven to a proper orientation in order to allow the smooth motion to the target. In these cases we propose a previous motion defining additional desired functions to be tracked. In our proposal, the desired trajectory of h_{33} do not change and we define the previous function to be tracked by h_{13} as follows

$$h_{13}^d(0 \leq t \leq T_1) = \frac{h_{13}(0)+h_{13}^d(T_1)}{2} + \frac{h_{13}(0)-h_{13}^d(T_1)}{2}\cos\left(\frac{\pi t}{T_1}\right) \tag{12}$$

As said, in $(0 \leq t \leq T_1)$ the goal is to regulate the orientation properly for the motion towards the target. For this purpose we have defined $h_{13}^d(T_1)$ proportionally to the initial value of h_{13} as $h_{13}^d(T_1) = -\frac{2}{3}h_{13}(0)$, which is the intermediate goal to be reached in T_1. Similar to the epipolar-based control we can detect if this previous phase (12) is required, and skipped otherwise.

Three simulations with this control law are shown in Fig. 5. The desired trajectories of h_{13} and h_{33} are shown with the resultant paths. It can be seen that the homography elements evolve accordingly to their desired values and the robot reaches properly the target position performing a smooth motion. This control law has the drawback that it fails if no plane is detected in the scene or if the plane detected has $n_z = 0$ (e. g. the horizontal ground plane). Nevertheless, when the robot is close to the target, with short baseline, the complete

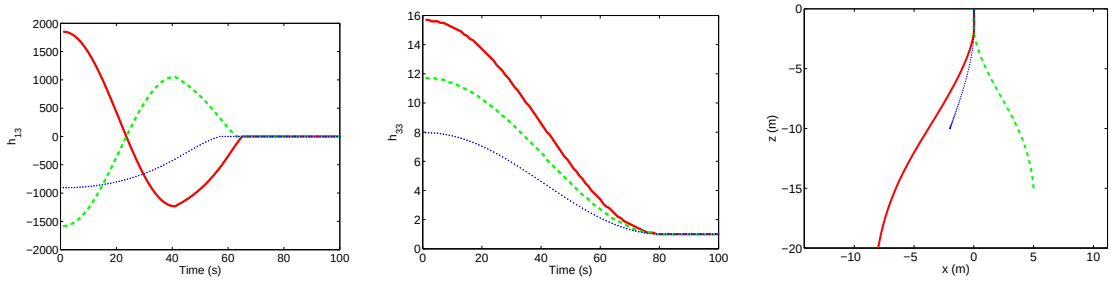

(a) h_{13} (b) h_{33} (c) Paths

Fig. 5. Evolution of h_{13} and h_{33} for three different initial positions and the resultant paths using the homography-based control law. The initial positions are $(-8, -20, -10°)$, $(5, -15, 5°)$ and $(-2, -10, -20°)$ while the target is in all the cases $(0, 0, 0°)$. Each of the simulations is drawn with a different line style.

scene becomes planar equivalent and this homography is useful for the control anyway. Therefore, the homography-based control law and the epipolar-based control law are complementary.

5 Switching Model-Based Control

Until now, two control laws have been defined, one is based on the epipolar geometry and the other on the homography model. Any of these previous control laws can fail when used alone due to degeneracies or particular cases. To overcome these problems we propose a switching control law which avoids the particular drawbacks of each control. Whenever a degenerate situation is detected, the system switches to the other controller. The key issue of handling with the switching strategy is that the controllers have been defined in such a way that the behaviour of the robot navigation is equivalent for both, and therefore switchings between controllers do not alter the resultant motion. Moreover, the switching control loop has been designed by taking into account that the switches do not generate discontinuities in the robot velocities, and therefore it performs a smooth motion.

The control loop of the approach presented is shown in the diagram of Fig. 6. An image in the current position is taken at each loop of the control. The features extracted from the current image are matched with the features of the target image. From the set of feature matches the fundamental matrix and the homography are estimated. Then, the control input $\boldsymbol{\nu}_F$ or $\boldsymbol{\nu}_H$ is computed from the current and desired parameter values (Table 1) and the control law gives the velocities that allow to track the desired trajectories of the epipoles or the homography elements. When the loop finishes the robot is in the target position and the current and target images are the same. One of the two individual control laws has to be selected along the time to be active, while

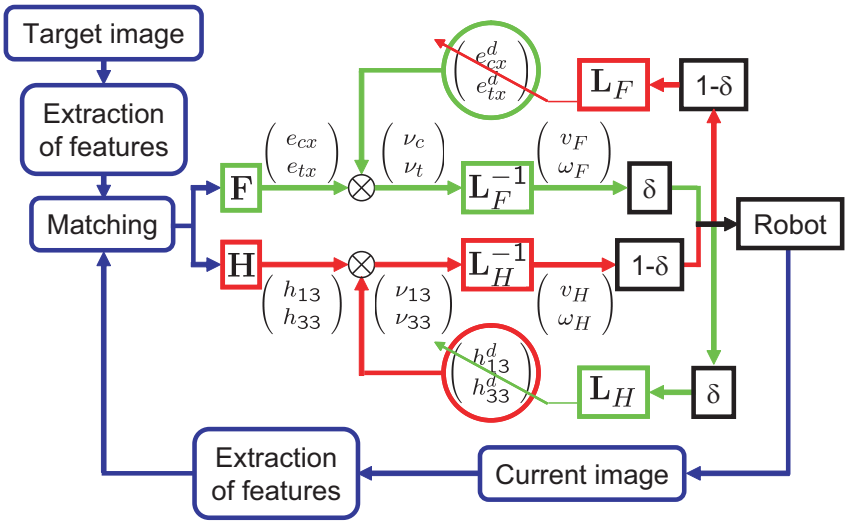

Fig. 6. Diagram of the switching control loop. The control scheme switches between the epipolar-based controller and the homography-based controller.

the other is inactive. For this purpose the parameter δ is defined as follows

$$\begin{cases} \delta = 1 \;\Rightarrow \text{Epipolar-based control active.} \\ \delta = 0 \;\Rightarrow \text{Homography-based control active.} \end{cases}$$

In order to guarantee smooth switchings between the controllers, the active controller gives feedback to the other controller to produce continuity in velocity when switched. Thus, during the control, the output velocities of the active controller are used to modify the desired trajectories of the input parameters of the unused control. When the control law is switched, because the model of the active control law becomes degenerated or ill-conditioned, the switch is performed without discontinuities in the robot velocities as the velocities given for both control laws when switching are the same. The modification of the desired trajectories of the non-active control law is carried out from the output velocities of the active control law by reversing the non-active control. For example, suppose the epipolar geometry-based control is active, $\delta = 1$ and (v_F, ω_F) are given to the robot as output of the control law (see Fig. 6). The output velocities (v_F, ω_F) are used to compute through L_H the values of the homography elements that would give the current velocities.

We have defined the switching control scheme and now, it remains to define the switching strategy for δ. For this purpose, degeneracies or ill-conditioned situations of each controller have to be detected properly. The issue of model selection or detecting degenerate situations has been addressed previously in [31]. This work presents strategies for tackling the problem of degeneracy for structure and motion recovery by using a statistical model selection test. In our approach, as we compute the fundamental matrix and a homography

simultaneously, two possibilities for the control selection have been considered. In the first we choose the best model in terms of inliers or residuals. Having a plane detected, the second possibility is by measuring the parallax of the points that do not fit the homography to detect if the scene is planar and then the epipoles are ill-conditioned.

6 Stability Analysis

In this section we analyze the stability of the proposed control by means of the *Lyapunov's Direct Method* [28]. Proposition 6.1 studies individually the stability of each control law. The stability of the switching control scheme is analyzed in Proposition 6.2 by means of a common Lyapunov function. Proposition 6.3 shows that the target position is the only equilibrium of the system. Finally Theorem 6.4 states the asymptotic stability of the system.

Proposition 6.1 *Consider the system (1) under the epipolar-based control or the homography-based control. There are Lyapunov functions $V_F(\mathbf{x},t)$ and $V_H(\mathbf{x},t)$ for the system under the epipolar-based control and the homography-based control, respectively; and the equilibrium $\mathbf{x}=\mathbf{0}$ of the system is locally asymptotically stable for each of the individual controllers.*

Proof We define the candidate Lyapunov function by the squared error norm

$$V_*(\mathbf{x},t)=\frac{1}{2}||\mathbf{e}_*||^2\ , \tag{13}$$

where $*$ is F or H denoting which controller is used, with the errors $\mathbf{e}_F$ and $\mathbf{e}_H$ defined in Table 1. Next, we study if $\dot{V}_*(\mathbf{x},t)$ is negative definite. Denoting $(e^d_{cx}, e^d_{tx})^T$ or $(h^d_{13}, h^d_{33})^T$ as $\mathbf{D}_*$ and $\mathbf{k}_*$ the 2×2 positive gain matrixes as defined in Table 1, the Lyapunov candidate function derivative is

$$\begin{aligned}\dot{V}_* &= \mathbf{e}_*^T\,\dot{\mathbf{e}}_* = \mathbf{e}_*^T\,\left(\mathbf{L}_*(v_*,\ \omega_*)^T-\dot{\mathbf{D}}_*\right)=\mathbf{e}_*^T\,\left(\mathbf{L}_*\mathbf{L}_*^{-1}\boldsymbol{\nu}_*-\dot{\mathbf{D}}_*\right)\\ &=\mathbf{e}_*^T\,\left(\mathbf{L}_*\mathbf{L}_*^{-1}(\dot{\mathbf{D}}_*-\mathbf{k}_*\mathbf{e}_*)-\dot{\mathbf{D}}_*\right)\\ &=-\mathbf{k}_*\mathbf{e}_*^T\,\mathbf{L}_*\mathbf{L}_*^{-1}\,\mathbf{e}_*+\mathbf{e}_*^T\left(\mathbf{L}_*\mathbf{L}_*^{-1}-\mathbf{I}\right)\dot{\mathbf{D}}_*\end{aligned} \tag{14}$$

Thus, if the estimation of $\mathbf{L}_*^{-1}$ is not too coarse, the global asymptotic stability of each one of the controllers is ensured [32]. The region of stability is reduced to local because the workspace is limited by the field of view constraints of the system. □

We have defined a switched controller, and its stability is not guaranteed by the stability of the individual controllers.

Proposition 6.2 *Consider the system (1) under the switching control scheme. There is a common Lyapunov function $V(\mathbf{x},t)$ for both the epipolar and the homography-based controllers, defined as*

$$V(\mathbf{x},t) = V_x + V_z + V_\phi \ , \tag{15}$$

where $V_x = \frac{1}{2}(x-x^d)^2$, $V_z = \frac{1}{2}(z-z^d)^2$ and $V_\phi = \frac{1}{2}(\phi-\phi^d)^2$, with ($x^d$,$z^d$,$\phi^d$) the desired final state of the system. The equilibrium $\mathbf{x}=\mathbf{0}$ of the system is locally asymptotically stable under the switching control scheme.

Proof We analyze the common Lyapunov function (15) for both controllers, and $\dot{V}$ will be shown negative for all time giving the stability of the switched system [33]. The derivative $\dot{V}$ gives

$$\begin{aligned}\dot{V} &= \dot{V}_x + \dot{V}_z + \dot{V}_\phi \\ &= -(x-x^d)\, v\, \sin\phi + (z-z^d)\, v\, \cos\phi + (\phi-\phi^d)\,\omega \ .\end{aligned} \tag{16}$$

The function (16) needs to be studied depending on the initial robot position in each of the four quadrants of the reference system, having the origin in the target (Fig. 1). The range of the angle ψ for each quadrant is $\psi \in [0, -\pi/2)$ for the first, $\psi \in (0, \pi/2]$ for the second, $\psi \in (\pi/2, \pi]$ for the third and $\psi \in [-\pi/2, -\pi)$ for the fourth. The analysis of the sign of each term of $\dot{V}$ reveals that it is negative definite. We next develop in detail the case of the third quadrant being the analysis of the rest quadrants analogue [34].

We consider the robot in the third quadrant and therefore we have $x \leq 0$, $z \leq 0$, $\pi/2 < \psi \leq \pi$ (Fig. 1). There are two different situations for the input desired trajectories depending on the initial robot position ($t \leq T_1$ or $t > T_1$). We consider the case of $t > T_1$, being analogue the procedure for $t \leq T_1$, and then $\phi - \psi \geq 0$ with $\phi < 0$. The sign of the epipoles can be deduced from Fig. 2(b) as $e_{cx} < 0$ and $e_{tx} > 0$ (See example with dotted line in Fig. 3). The sign of the homography elements used in the control can be deduced from (9),

$$\begin{cases} h_{13} = \frac{\alpha_x}{\cos\psi}\left(\sin\phi\cos\psi + z\sin(\phi-\psi)\frac{n_z}{d_\pi}\right) \\ h_{33} = \frac{1}{\cos\psi}\left(\cos\phi\cos\psi + z\cos(\phi+\psi)\frac{n_z}{d_\pi}\right) \end{cases}$$

and it yields that $h_{13} < 0$ and $h_{33} > 0$ (See example with dotted line in Fig. 5). Taking into account the sign of the previous parameters with Table 1 and the desired evolution of the input (Sections 3.3 and 4.3) we can deduce $\nu_c > 0$, $\nu_t < 0$, $\nu_{13} > 0$ and $\nu_{33} < 0$. We can now study the sign of the velocities given by the controllers (Table 1) yielding ($v_F > 0$, $\omega_F > 0$) and ($v_H > 0$, $\omega_H > 0$). Finally, we can conclude taking into account these results that (16) is

negative definite in the third quadrant at $t > T_1$. The same procedure repeated for each quadrant leads to $\dot{V} < 0$ in all the workspace, which is limited by the field of view constraints of the system [34]. Therefore, the system is locally asymptotically stable under the switching control scheme. □

In our system the equilibrium state of the system is $\mathbf{x} = (x^d, z^d, \phi^d) = \mathbf{0}$. In nonlinear systems there can be one or more equilibrium states and we need to prove that the target position is the only equilibrium state of the system.

Proposition 6.3 *The desired target position* $\mathbf{x} = \mathbf{0}$ *is the equilibrium state of the system and then* $\mathbf{x} = (x, z, \phi) = \mathbf{0} \Leftrightarrow (v, \omega) = (0, 0)$.

Proof The desired final value for the epipoles to be tracked in the epipolar-based control is zero. Thus, when this control finish we have from (3) that $(e_{cx}, e_{tx}) = (0, 0) \Leftrightarrow (x, z, \phi) = (0, z, 0)$. Therefore, the x-coordinate and the orientation are corrected but not the depth. Then, the equilibrium state is any point along the z-axis. Nevertheless, at the end of the motion the control will always switch to the homography-based control in order to avoid the fundamental matrix degeneracy with short baseline. It is known that $(x, z, \phi) = (0, 0, 0) \Leftrightarrow \mathbf{H} = \mathbf{I}$. Using the homography-based control law, we have at the end of motion $h_{13} = 0$, $h_{33} = 1$ and $(v, \omega) = (0, 0)$. From the tracked trajectories, we have that $h_{13} = 0$ implies $\psi = 0$ and $x = 0$ (see Fig. 1). Taking this into account it can be proved that, having $h_{13} = 0$ and $h_{33} = 1$, if $x = 0$ or $z = 0$ or $\phi = 0$ then $\mathbf{H} = \mathbf{I}$. The demonstration is straightforward from (9). Therefore, the equilibrium of the system is $\mathbf{x} = \mathbf{0}$. □

Theorem 6.4 *Consider the system (1) to be controlled by the switching control scheme presented. The target position is the only equilibrium state of the system and it is locally asymptotically stable.*

Proof This result follows directly from the previous propositions. The stability of each control law, epipolar-based and homography-based, is proved in Proposition 6.1. Even if each control law is stable, the stability of the global control scheme needs to be demonstrated. This is analyzed in Proposition 6.2 by using a common Lyapunov function. Finally we have shown in Proposition 6.3 that there is only one equilibrium of the system and it is the target location. Thus, the stability analysis shows that the system is locally asymptotically stable. □

7 Experimental Validation

In this section we present the experimental validation of the switching control scheme. Experiments with simulated data and experiments with a real

platform are given to show the performance of the approach.

7.1 Simulation Results

The simulated data are a set of points projected into the camera image plane, where the size of the virtual image is 640×480 pixels. The scene consists of a cloud of 3D points randomly distributed and a set of points belonging to a plane. Simulations of Fig. 7 show two extreme situations presenting the evolution of the control input parameters and the resultant path. The initial position in these simulations is $(-2, -10, -20^\circ)$ and the target position is $(0, 0, 0^\circ)$. In the first case the scene is totally planar and the computed epipoles become unstable (Fig. 7 (a,b)), while the homography behaves properly as expected (Fig. 7 (c,d)). Therefore the homography-based control is used during all the navigation ($\delta = 0$). The other case is when a general scene without a dominant plane is seen by the camera and then, the homography becomes useless Fig. 7 (c',d') and the epipolar-based control is used ($\delta = 1$). However, at the end of the motion, the epipoles degenerate because of short baseline and the homography control becomes useful to switch with (see Fig. 7 (a',b') for approximately $t > 80s$). This is because, when the baseline is small, the homography is defined by a rotation, independently of the scene observed. In general, the scenes found in practice are not so extreme. Thus, it would be easy to find a more or less good plane despite it is no dominant or, in a planar scene, it should not be difficult to find objects not belonging to the plane. Therefore, the task of the switching control strategy is to select the best model in each moment of the navigation. The velocities computed by the controllers are shown in Fig. 7 (e,e').

Next, we present a simulation showing the performance of the control with several switches. Three simulations of the switching control law are superposed in Fig. 8 with different initial positions. These initial positions are $(-8, -20, -10^\circ)$, $(5, -15, 5^\circ)$ and $(-2, -10, -20^\circ)$ while the target is in all the cases $(0, 0, 0^\circ)$. Several arbitrary switches are carried out to show the performance of the system with control switches. This model selection is given by δ which is shown in Fig. 8 (a). It can be seen that the resultant motion is not affected by the control switches. The evolution of the control input parameters of the inactive control has small variations compared with its desired designed trajectories. These can be easily seen after each switch. This is because the desired trajectories of the inactive control are adapted for giving the same output as the active control, guaranteing continuity in the switches. The evolution of the epipoles clearly shows the degeneracy of the epipolar geometry due to short baseline at the end of the motion.

The simulations of Fig. 9 show the performance of the switching control when

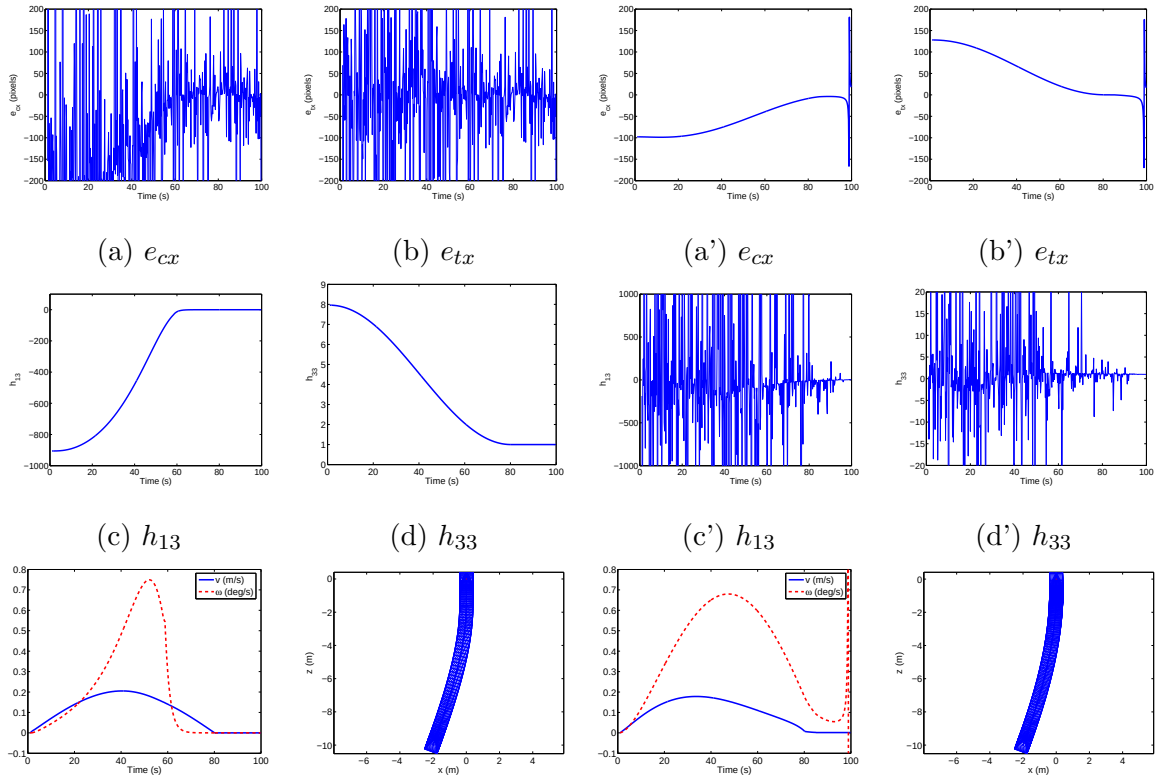

(a) e_{cx} (b) e_{tx} (a') e_{cx} (b') e_{tx}

(c) h_{13} (d) h_{33} (c') h_{13} (d') h_{33}

(e) (v_H, ω_H) (f) Path (e') (v_F, ω_F) (f') Path

Fig. 7. (a-f) Simulation of the switching control with a planar scene. (a'-f') Simulation of the switching control without a dominant plane in the scene.

there is noise in the coordinates of image points. The control law starts with the epipolar geometry-based control and when it becomes ill-conditioned the control switches to the homography-based control. From results of Fig. 9, it can be seen that the method converges properly in spite of image noise. Note that at the end of the motion the epipoles become totally unstable due to short baseline and, on the other hand, the homography becomes more robust against noise as the robot reaches the target position.

The unknown focal length parameter α_x of the calibration matrix appears in the controller. Moreover, we have assumed that the principal point is in the centre of the image. We show now the performance of the control associated with the uncertainty in these parameters. In Fig. 10 (a) the value of the focal length of the homography control law has been fixed to $f = 6\,mm$. Then, its real value is modified to see the final position error. It can be seen that the performance of the method is not affected except when the real focal length tends to zero. The value of x_0 used in the homography control is zero, while its real value is changed (Fig. 10 (b)). It can be seen that higher error in the estimation of x_0 produces higher error in the final lateral and orientation values. It can also be seen that the errors in x and ϕ are coupled. However, we can assume in practice that the estimation error of x_0 is small and then, it

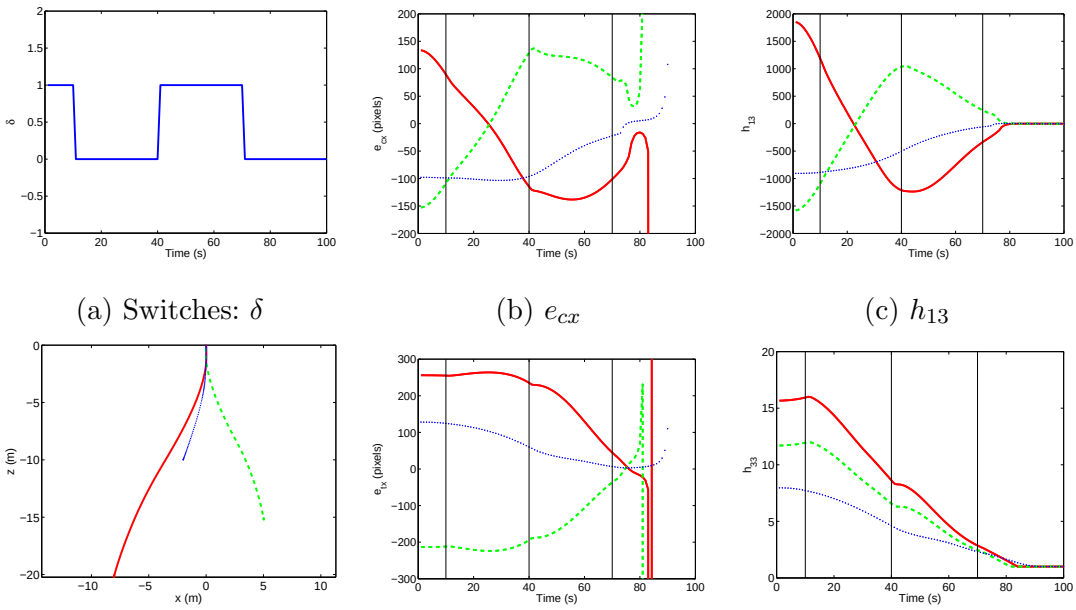

(a) Switches: δ (b) e_{cx} (c) h_{13}

(d) Paths (e) e_{tx} (f) h_{33}

Fig. 8. Simulations for three different initial positions to test the effect of arbitrary switches. The switching sequence is defined by δ (if $\delta = 1$ the epipolar-based control is active).

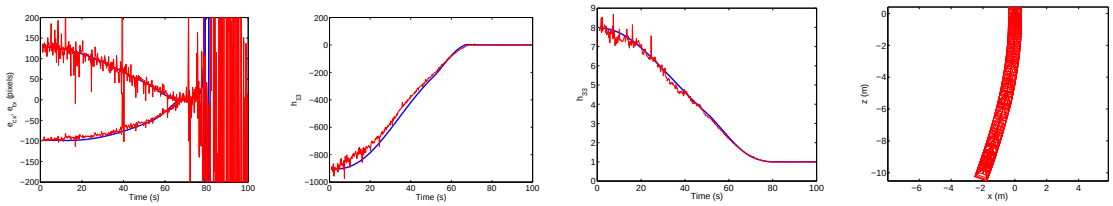

(a) e_{cx} and e_{tx} (b) h_{13} (c) h_{33} (d) Path

Fig. 9. Simulation of the switching control without noise (thick line) and with image noise of $\sigma = 1$ pixel (thin line). The initial position is $(x, z, \phi) = (-2, -10, -20^\circ)$ and the target $(0, 0, 0^\circ)$. In (a), e_{cx} is the negative plot and e_{tx} the positive. The robot path with image noise is shown in (d).

produces small final position errors that can be disregarded. These simulations are carried out using the homography-based control. The performance of the epipolar-based control is similar with respect to α_x and x_0 uncertainty. Results show that no specific calibration is needed for the convergence of the system.

The distance between the current and target camera ρ is unknown (Table 1), but it is replaced with a constant parameter without affecting the convergence of the control system. In fact it behaves as a constant gain of the forward velocity v_F which is compensated by the control law because of the feedback action of the control loop. To check the correct behaviour of the system against the fixed value of the unknown ρ, we have tested with values of ρ from centimeters

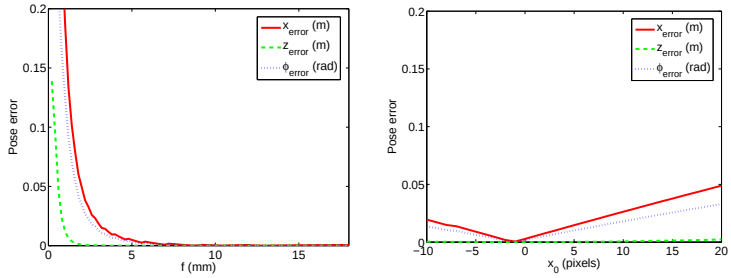

(a) (b)

Fig. 10. Final position error in (x, z, ϕ) when varying the camera calibration parameters: focal length (a) and principal point coordinates (b).

to dozens of meters for the same initial real distance of 10 meters. The only difference obtained is a proportional variation in the time needed for completing the experiment, without affecting the final error. This approach does not compute the decomposition of the homography, therefore, neither the value of the normal to the plane ($\mathbf{n}$) nor the distance to it (d_π) are known. We have considered the constant parameter d_π/n_z as a gain of the control. We have tested the effect of the uncertainty in n_z and d_π on the performance of the control. Simulations have been performed by fixing the real values of n_z and d_π while the values used in the control are modified. The results show that the convergence of the method is not affected and good final position errors are obtained. However, the homography-based control fails as expected if the real plane is too close to the target position ($d_\pi \to 0$) or if the component n_z of the normal vector is small ($n_z \to 0$).

Simulations showing the robot motion together with the evolution of the control parameters are shown in the video attachment (**Video1**).

7.2 Real World Experiments

The experimental platform is a Pioneer P3-DX from ActivMedia (Fig. 1(a)). It has a nonholonomic differential drive base with a rear caster wheel. The robot is equipped with a Canon VC-C4 pan-tilt-zoom CCD camera mounted on top. There is a computer onboard with operating system Debian Linux and the program communicates with the robot and the camera using Player [2].

The extraction and matching of image points is carried out using SURF features. SURF [3] (Speeded Up Robust Features) is an interest point detector and descriptor which is invariant to scale and rotation [35]. This descriptor is

[2] The Player Project creates free software tools for robot and sensor applications. `http://playerstage.sourceforge.net/`

[3] The SURF library is available online: `http://www.vision.ee.ethz.ch/~surf/`

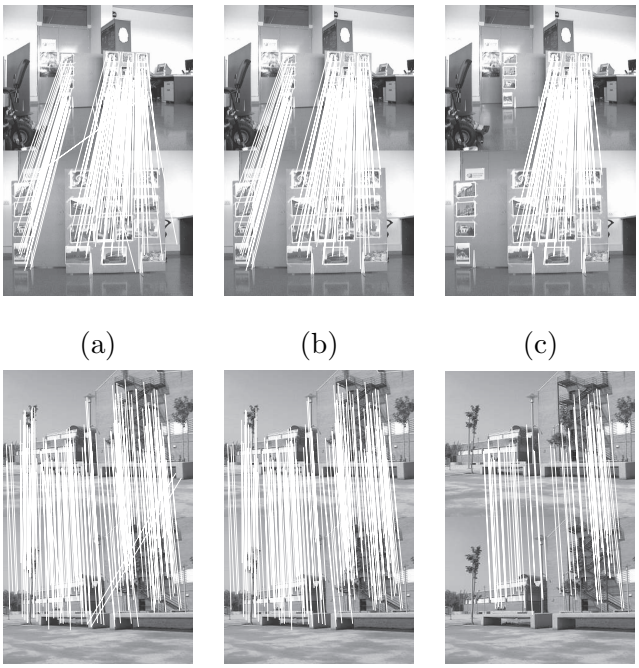

Fig. 11. Two examples indoor and outdoor of matches from SURF features (a,d) between a current (top) and a target image (bottom). Matches left after fundamental matrix estimation (b,e). Matches left after homography estimation (c,f).

quite similar to the well-known SIFT [36] with respect to repeatability, distinctiveness, and robustness, however, it can be computed faster. An example of the matching process is shown in Fig. 11, where the white lines join matched points. It is assumed that the putative matches obtained from the SURF features include mismatches. Thus, the fundamental matrix and the homography are estimated with RANSAC [37]. The estimation of the homography and the epipolar geometry is programmed using the OpenCV library [4] . The size of the images taken by the camera in the experiments is 480×240 pixels, a higher resolution increases too much the computing time and a lower resolution reduces the accuracy of the geometric model estimations. In our experiments, the control loop runs currently at $0.75Hz$ which is actually slow, but even in this way the control works successfully.

The results of a real experiment using the switching model-based control law are given in Fig. 12. The resultant robot path given by the odometry is shown Fig. 12 (c), and the final error obtained is 4 cm in x and 1 cm in z. As expected the epipolar geometry degenerates as the robot reaches the target and the epipoles become unstable (Fig. 12 (a,d), approximately at $t > 70s$). The navigation starts using the epipolar-based controller and it is switched

[4] The Open Computer Vision Library is a collection of algorithms for computer vision problems. `http://www.intel.com/technology/computing/opencv/`

to the homography-based controller in $t_s = 70.4s$. The criteria for the switching strategy is to check the evolution of the epipoles, if the epipoles change suddenly over a threshold they can be considered unstable and the switch to the homography model is done. The number of matches obtained during the navigation is shown in Fig. 12 (f), as the robot moves towards the target the number of matches increases. Last row of Fig. 12 show the initial image, the target image and the image at the end of the motion. In these experiments we have imposed the control selection strategy starting with the epipolar-based control and switching when the epipoles become unstable to the homography based-control. This is the more common situation because usually the fundamental matrix works well far from the target, while the homography is more robust near the target. It is usual that any of the geometric models can be used to be active in the switching control law at some point in the navigation, for example, during ($20s < t < 70s$) both the epipolar Fig. 12 (a,d) and the homography-based Fig. 12 (b,e) controllers would work correctly. This confirms that a simple switching strategy is enough and its selection is not critical in practice. The video attachment **Video2** shows a real experiment from a external video camera. The robot in the target position, where the reference image was taken, is overlaid over the video.

8 Conclusion

In this paper we have presented a new visual control approach for mobile robots with nonholonomic motion constraints. The switching control law designed consists of two different controllers, one is based on the epipolar geometry and the other on the homography model. This is an image-based approach which does not need to compute the robot position, depth or 3D information of the scene. Each controller is defined by an exact input-output linearization of the correspondent geometric model and the desired trajectories of the input are defined by means of sinusoids. The advantage of the control switching is that degeneracies or ill-conditioned situations of each model are avoided, allowing the robust navigation of the robot to the target position. Experimental validation shows that the control performs properly with the switches between the models, resulting in a smooth motion of the robot. Simulations and experiments with a real platform show that the method is robust and can cope with image noise and uncertainty of the control parameters.

References

[1] G. N. DeSouza and A. C. Kak, "Vision for mobile robot navigation: A survey," *IEEE Transactions on Pattern Analysis and Machine Intelligence*, vol. 24, no. 2,

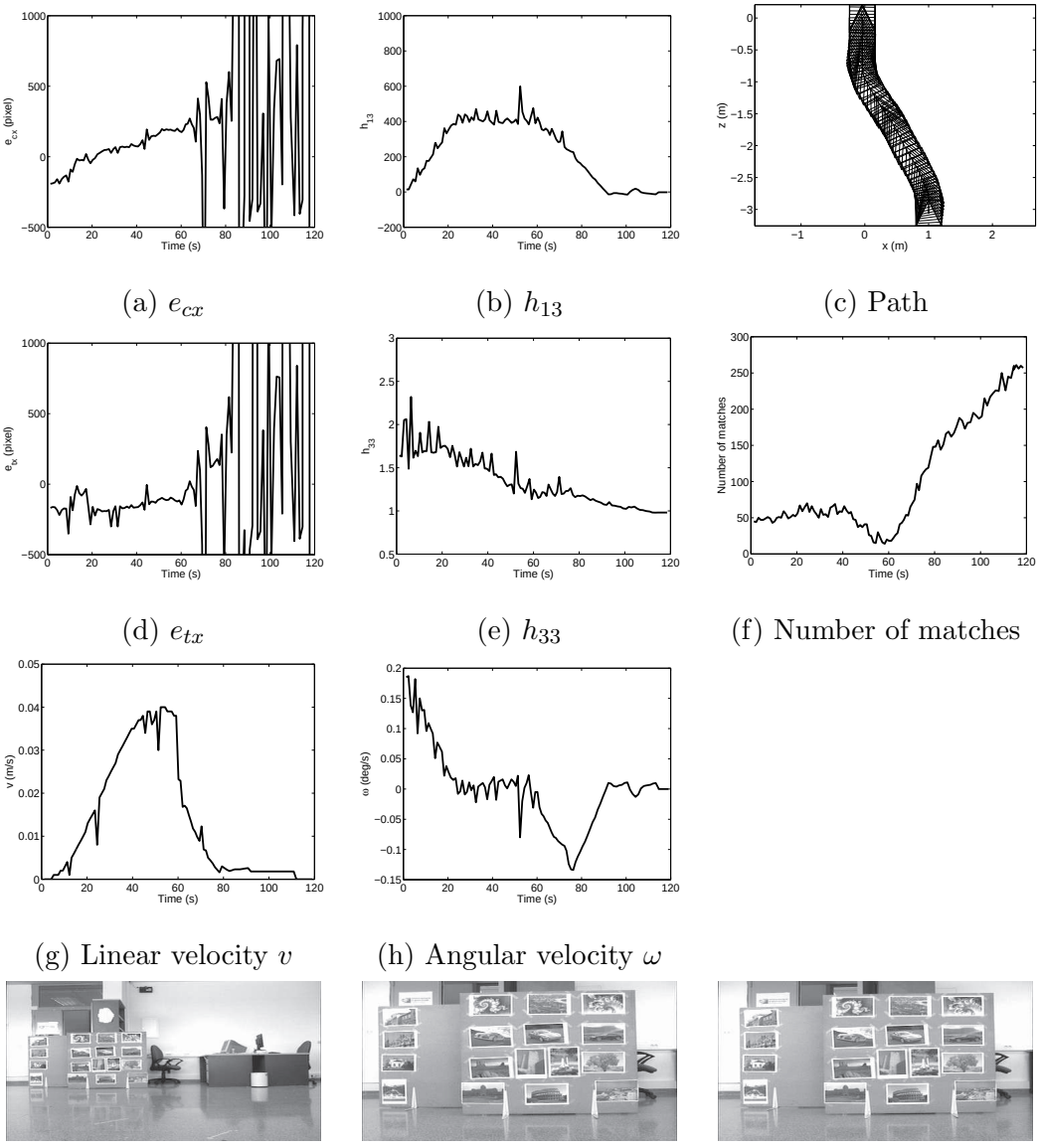

(a) e_{cx} (b) h_{13} (c) Path

(d) e_{tx} (e) h_{33} (f) Number of matches

(g) Linear velocity v (h) Angular velocity ω

Initial image Target image Final image

Fig. 12. Real experiment with start position at $(x, z, \phi) = (1, -3, 0°)$ and target position at $(0, 0, 0°)$. The control selection is given by $\delta(t \leq t_s) = 1$ and $\delta(t > t_s) = 0$ with $t_s = 70.4s$.

pp. 237–267, 2002.

[2] S. Hutchinson, G. D. Hager, and P. I. Corke, "A tutorial on visual servo control," *IEEE Tran. on Robotics and Automation*, vol. 12, no. 5, pp. 651–670, 1996.

[3] Y. Ma, J. Kosecká, and S. Sastry, "Vision guided navigation for a nonholonomic mobile robot," in *Proceedings of the 36th IEEE CDC*, 1996, pp. 3069–3074.

[4] K. Deguchi, "Optimal motion control for image-based visual servoing by decoupling translation and rotation," in *IEEE/RSJ International Conference on Intelligent Robots and Systems*, 1998, pp. 705–711.

[5] I. H. Suha and T. W. Kim, "A visual servoing algorithm using fuzzy logics and fuzzy-neural networks," *Mechatronics*, no. 10, pp. 1–18, 2000.

[6] F. Conticelli and B. Allotta, "Nonlinear controllability and stability analysis of adaptive image-based systems," *IEEE Transactions on Robotics and Automation*, vol. 17, no. 2, pp. 208–214, 2001.

[7] J. J. Guerrero and C. Sagüés, "Uncalibrated vision based on lines for robot navigation," *Mechatronics*, vol. 11, no. 6, pp. 759–777, Sept. 2001.

[8] A. A. Argyros, K. E. Bekris, S. C. Orphanoudakis, and L. E. Kavraki, "Robot homing by exploiting panoramic vision," *Autonomous Robots*, vol. 19, no. 1, pp. 7–25, 2005.

[9] S. Benhimane and E. Malis, "Homography-based 2D visual servoing," in *IEEE International Conference on Robotics and Automation*, 2006, pp. 2397–2402.

[10] Z. Chen and S. T. Birchfield, "Qualitative Vision-Based Mobile Robot Navigation," in *IEEE International Conference on Robotics and Automation*, 2006, pp. 2686–2692.

[11] R. Basri, E. Rivlin, and I. Shimshoni, "Visual homing: Surfing on the epipoles," *International Journal of Computer Vision*, vol. 33, no. 2, pp. 117–137, 1999.

[12] B. Liang and N. Pears, "Visual navigation using planar homographies," in *IEEE Conference on Robotics and Automation*, 2002, pp. 205–210.

[13] S. Benhimane, E. Malis, P. Rives, and J. R. Azinheira, "Vision-based control for car platooning using homography decomposition," in *IEEE Int. Conference on Robotics and Automation, Barcelona, Spain*, April 2005, pp. 2173–2178.

[14] T. Drummond and R. Cipolla, "Application of Lie algebras to visual servoing," *International Journal of Computer Vision*, vol. 37, no. 1, pp. 21–41, 2000.

[15] Y. Fang, W. E. Dixon, D. M. Dawson, and P. Chawda, "Homography-based visual servo regulation of mobile robots," *IEEE Transactions on Systems, Man, and Cybernetics, Part B*, vol. 35, no. 5, pp. 1041–1050, 2005.

[16] E. Malis, F. Chaumette, and S. Boudet, "2 1/2 D visual servoing," *IEEE Tran. on Robotics and Automation*, vol. 15, no. 2, pp. 234–246, Apr. 1999.

[17] P. Rives, "Visual servoing based on epipolar geometry," in *IEEE/RSJ Int. Conference on Intelligent Robots and Systems*, vol. 1, 2000, pp. 602–607.

[18] G. López-Nicolás, C. Sagüés, J. J. Guerrero, D. Kragic, and P. Jensfelt, "Nonholonomic epipolar visual servoing," *IEEE International Conference on Robotics and Automation*, pp. 2378–2384, 2006.

[19] G. L. Mariottini, G. Oriolo, and D. Prattichizzo, "Image-based visual servoing for nonholonomic mobile robots using epipolar geometry," *IEEE Transactions on Robotics*, vol. 23, no. 1, pp. 87–100, 2007.

[20] H. Zhang and J. P. Ostrowski, "Visual motion planning for mobile robots," *IEEE Tran. on Robotics and Automation*, vol. 18, no. 2, pp. 199–208, 2002.

[21] N. R. Gans and S. A. Hutchinson, "A stable vision-based control scheme for nonholonomic vehicles to keep a landmark in the field of view," in *IEEE Int. Conference on Robotics and Automation*, Apr. 2007, pp. 2196–2200.

[22] E. Malis and F. Chaumette, "2 1/2 D visual servoing with respect to unknown objects through a new estimation scheme of camera displacement," *International Journal of Computer Vision*, vol. 37, no. 1, pp. 79–97, 2000.

[23] G. López-Nicolás, C. Sagüés, J. J. Guerrero, D. Kragic, and P. Jensfelt, "Switching visual control based on epipoles for mobile robots," *Robotics and Autonomous Systems*, vol. 56, no. 7, pp. 592–603, 2008.

[24] G. L. Mariottini, D. Prattichizzo, and G. Oriolo, "Epipole-based visual servoing for nonholonomic mobile robots," *IEEE International Conference on Robotics and Automation*, pp. 497–503, 2004.

[25] G. López-Nicolás, C. Sagüés, and J. J. Guerrero, "Homography-based visual control of nonholonomic vehicles," in *IEEE International Conference on Robotics and Automation*, Apr. 2007, pp. 1703–1708.

[26] R. I. Hartley and A. Zisserman, *Multiple View Geometry in Computer Vision*, 2nd ed. Cambridge University Press, 2004.

[27] A. Isidori, *Nonlinear Control Systems*. Springer, 1995.

[28] J.-J. E. Slotine and W. Li, *Applied nonlinear control*. Prentice Hall, Englewood Cliffs NJ, 1991.

[29] R. Murray and S. Sastry, "Nonholonomic motion planning: Steering using sinusoids," *IEEE Transactions on Automatic Control*, vol. 38, no. 5, pp. 700–716, 1993.

[30] G. López-Nicolás, C. Sagüés, and J. J. Guerrero, *Shortest Path Homography-Based Visual Control for Differential Drive Robots*. G. Obinata and A. Dutta Eds. Vision Systems, I-Tech Education and Pub., Austria. 2007. pp. 583–596.

[31] P. H. S. Torr, A. Fitzgibbon, and A. Zisserman, "The problem of degeneracy in structure and motion recovery from uncalibrated image sequences," *International Journal of Computer Vision*, vol. 32, no. 1, pp. 27–45, 1999.

[32] F. Chaumette and S. Hutchinson, "Visual servo control, part I: Basic approaches," *IEEE Robotics and Automation Magazine*, vol. 13, no. 4, pp. 82–90, Dec. 2006.

[33] D. Liberzon, *Switching in Systems and Control*. Birkhauser, 2003.

[34] G. López-Nicolás, *Visual Control of Mobile Robots through Multiple View Geometry*. PhD Dissertation, Universidad de Zaragoza, 2008.

[35] H. Bay, T. Tuytelaars, and L. Van Gool, "SURF: Speeded up robust features," in *Proceedings of the 9th European Conference on Computer Vision*, vol. 3951, May 2006, pp. 404–417.

[36] D. Lowe, "Distinctive image features from scale-invariant keypoints," *International Journal of Computer Vision*, vol. 60, no. 2, pp. 91–110, 2004.

[37] M. A. Fischler and R. C. Bolles, "Random sample consensus: a paradigm for model fitting with applications to image analysis and automated cartography," *Commun. ACM*, vol. 24, no. 6, pp. 381–395, 1981.